processes

MDPI

Article

Hybrid Plasma-Catalytic CO_2 Dissociation over Basic Metal Oxides Combined with CeO_2

Oleg Golubev * and Anton Maximov

A.V. Topchiev Institute of Petrochemical Synthesis, Russian Academy of Sciences (TIPS RAS), 119991 Moscow, Russia; max@ips.ac.ru

* Correspondence: golubev@ips.ac.ru

Abstract: The problem of CO_2 waste in the atmosphere is a major concern, and methods of CO_2 utilization are being currently developed. In the present work, a plasma-catalytic process is applied for CO_2 dissociation. A series of MgO and CeO_2-containing catalysts were synthesized, and the samples were characterized by: a low-temperature N_2 adsorption-desorption analysis, X-ray diffraction, X-ray photoelectron spectroscopy, temperature-programmed desorption of CO_2, and X-ray fluorescence spectroscopy. It was stated that under dielectric barrier discharge conditions, the catalyst surface, composition, and phase content remain unchanged. The superior catalytic activity of the MgCe-Al sample is attributed to the combination of weak basic sites and oxygen vacancies on the catalyst surface.

Keywords: plasma catalysis; CO_2 utilization; oxygen vacancies; basic oxides; dielectric barrier discharge

check for updates

Citation: Golubev, O.; Maximov, A. Hybrid Plasma-Catalytic CO_2 Dissociation over Basic Metal Oxides Combined with CeO_2. *Processes* **2023**, *11*, 1553. https://doi.org/10.3390/pr11051553

Academic Editors: Chundong Zhang and Ruxing Gao

Received: 25 April 2023
Revised: 12 May 2023
Accepted: 17 May 2023
Published: 18 May 2023

1. Introduction

The increasing concentration of carbon dioxide (CO_2) in the atmosphere is recognized as one of the major contributors to global warming and climate change. The current levels of CO_2 are unprecedented in human history, and they have been increasing at an alarming rate over the past few decades [1]. The consequences of this trend are already visible in the form of rising sea levels, more frequent extreme weather events, and biodiversity loss, among others [2]. Therefore, finding efficient ways to reduce CO_2 emissions and mitigate its harmful effects has become a major challenge for scientists globally.

One promising approach is to use CO_2 as a feedstock to produce valuable chemicals, fuels, and materials through various chemical transformations. This concept, known as carbon capture and utilization (CCU), has gained significant attention in recent years due to its potential to address both the environmental and economic challenges associated with CO_2 emissions.

Traditional methods for CO_2 utilization include chemical and biological processes, such as chemical absorption [3], catalytic hydrogenation [4], and microbial conversion [5]. However, these methods suffer from low conversion efficiency, high consumption of energy, and limited scalability. Therefore, there is a need to explore new and innovative approaches that can overcome these limitations and enable the sustainable utilization of CO_2.

Plasma-catalytic decomposition of CO_2 is a promising alternative, which combines the advantages of both plasma and catalysis to achieve high conversion rates and selectivity. Plasma can provide the high-energy electrons, ions, and radicals needed to activate CO_2 molecules [6–8], while catalysts can enhance the adsorption, activation, and reaction of CO_2 on their surfaces [9–11]. Moreover, plasma-catalytic systems can be operated at ambient conditions, making them more energy-efficient and environmentally friendly than traditional methods.

Barrier discharge or dielectric barrier discharge (DBD) is commonly used for the plasma-assisted catalytic decomposition of CO_2 due to the simplicity of the reactor and low operating temperature (from 20 to 150 °C) [12–14]. Such a plasma-catalytic setup consists

of two coaxial electrodes, between which the electric discharge is generated [15,16]. The catalytic material is packed between the electrodes (in the discharge zone), so the plasma and catalyst may interact with each other. The micro-discharges, which are generated between the catalyst particles, may modify the catalyst properties [17]. To achieve efficient plasma-catalytic decomposition of CO_2, various catalysts and dielectric materials have been applied to barrier discharge. For instance, CO_2 conversion was enhanced in the presence of $BaTiO_3$ or $CaTiO_3$ [18–21], which is explained by the higher plasma electron density inside the packed bed. In fact, such materials play a more "discharge modifier" role rather than "catalytic". In a traditional meaning, two main groups of substances are attractive as potential catalysts. One of them is a group of metal oxides possessing oxygen vacations in the structure, e.g., CeO_2, which has gained much attention as a catalyst due to its crystal defects and oxygen storage capacity [22]. Such properties make it possible to conduct various catalytic reactions involving CeO_2, such as methanol oxidation [23], CO_2 reduction [24], water splitting [25], various photocatalytic reactions [26], diesel soot abatement [27], and many more. When introduced inside the CeO_2-packed discharge zone during plasma-catalytic CO_2 dissociation, the carbon dioxide molecule is activated by plasma electrons. Then the molecule is adsorbed by the oxygen vacancy V_o of the CeO_2 catalyst with consequent C=O bond cleavage producing CO. The oxygen atom adsorbed on the vacancy is then desorbed from the catalyst surface; the catalytic cycle is repeated [28].

Another type of catalytic substance for plasma-catalytic CO_2 dissociation is metal oxides with basic properties (e.g., MgO, CaO). Since CO_2 is an acidic oxide, it reacts readily with molecules possessing basic properties. Basic sites of MgO and CaO may enhance the CO_2 chemisorption on the catalyst surface and therefore raise the plasma-catalytic CO_2 conversion [29–31].

A combination of two types of oxides (CeO_2 with oxygen vacancies and basic metal oxides) in a single catalyst may be useful, as it would enhance the CO_2 adsorption on the catalyst surface with subsequent decomposition. However, no study on the synthesis and plasma-catalytic properties has been reported in the literature currently. To reveal the possible synergetic effect for plasma-catalytic CO_2 decomposition, we studied combined $MgO–CeO_2$ and $CaO–CeO_2$ catalysts. Our group has conducted a preliminary study, which showed the advantage of such a catalyst compared with a mono-oxide catalyst [32]. In the present work, we aim to investigate the plasma-catalytic CO_2 decomposition process in the presence of MgO and CaO-promoted CeO_2 catalysts. The main goal of this study is to establish the key characteristics, which determine the activity and stability of such catalysts.

2. Materials and Methods

2.1. Materials

All reagents were purchased from commercial suppliers and used without further purification. Cerium nitrate (LLC "Tsentr Tekhnologyi Lantan", 99%), magnesium acetate (JSC "Vekton", 99%), and calcium nitrate (JSC "Lenreaktiv", 98.5%) were used as metal oxides precursors. Metal salt solutions were impregnated on a γ-Al_2O_3 support (0.63–1.00 mm fraction), which was obtained by the extrusion of Pural SB boehmite (Sasol, 99%). CO_2 (JSC "Moscow Gas Refinery Plant", 99.5%) was used as a feed, and Ar (JSC "Moscow Gas Refinery Plant", 99.993%) was used as a carrier gas in the gas chromatograph.

2.2. Catalysts Preparation

Catalysts were prepared using the wetness impregnation technique. In a typical synthesis, 2.29 g of Ce nitrate was dissolved in 7.3 cm^3 of distilled water and added to the 8.1 g of γ-Al_2O_3 support. The impregnated support was dried at 60 °C for 2 h, 80 °C for 2 h, 90 °C for 2 h, 100 °C for 2 h, and then calcined in a muffle furnace at 400 °C for 3 h. Catalysts with two metal oxides ($MgO–CeO_2$ and $CaO–CeO_2$) were prepared using a two-step impregnation procedure. In the first step, CeO_2/Al_2O_3 was prepared similarly to the technique described above. Then, CeO_2/Al_2O_3 was impregnated with a solution of a

second metal salt with further drying and calcination. The catalysts prepared were denoted as follows (Table 1).

Table 1. The denotation of prepared catalysts.

Catalyst Composition	Denotation
Al_2O_3	Al
CeO_2 (10 wt.%)/Al_2O_3	Ce–Al
CeO_2 (20 wt.%)/Al_2O_3	Ce20–Al
MgO (10 wt.%)/Al_2O_3	Mg–Al
MgO (10 wt.%)–CeO_2 (10 wt.%)/Al_2O_3	MgCe–Al
CaO (10 wt.%)–CeO_2 (10 wt.%)/Al_2O_3	CaCe–Al

2.3. Catalysts Characterization

The surface characteristics (S_{BET}, V_{pores}, d_{pores}) were determined using a Belsorp miniX (Microtrac MRB) instrument. Before analysis, the samples were degassed at 300 °C and 10 Pa for 8 h. To calculate the surface area, the BET method was applied with adsorption data in the range of relative pressures (P/P_0) of 0.05−0.20. The total pore volume was calculated based on the amount of adsorbed nitrogen at a relative pressure P/P_0 = 0.95.

Powder X-ray diffraction (XRD) was used to determine the phase composition of the catalysts. The X-ray diffractograms were obtained for a range of 10–100° 2θ by using a Rigaku Rotaflex RU-200 diffractometer (CuK_α radiation) equipped with a Rigaku D/Max-RC goniometer (a rotation speed of 1°/min; a step 0.04°). The identification of diffractograms was carried out using the PDF-2 ICDD database of powder diffraction patterns.

The average size (D) of crystallites was calculated by the Scherrer equation:

$$D = \frac{K\lambda}{\beta \cos \theta} \quad (1)$$

where D is the crystallite size, λ is the wavelength of the Cu–Kα radiation, K is a constant and its value is taken as 0.9, θ is the diffraction angle [rad], and β is the full-width at half maximum (FWHM) [rad].

The X-ray photoelectron spectroscopy (XPS) measurements were performed using a «PREVAC EA15» electron spectrometer. In the current work, AlKα (hν = 1486.74 eV, 150 W) was used as a primary radiation source. The pressure in the analytical chamber did not exceed 5×10^{-9} mbar during the spectra acquisition. The binding energy scale was pre-calibrated using the positions of Ag3d5/2 (368.3 eV) and Au4f7/2 (84.0 eV) from silver and gold foils, respectively. The peaks were deconvoluted using PeakFit software set to the Shirley background subtraction, followed by peak fitting to Voigt functions with an 80% Gaussian and 20% Lorentzian character.

The content of elements (Al, Si, Ce, Mg, Ca) was measured with an X-ray fluorescence spectrometer: ARL Perform'x Sequential XFR (Thermo Fisher Scientific, Waltham, MA, USA) equipped with 2500 W X-ray tube. Before analysis, the samples were ground and pressed into a tablet with H_3BO_3.

The basicity of the catalysts was determined by the CO_2-temperature programmed desorption (TPD-CO_2) method using USGA-101 (LLC "Unisit") equipment. The catalyst sample was placed into a quartz reactor and treated in a flow of He (JSC "Moscow Gas Refinery Plant", 99.995%) at 512 °C for 40 min to remove water and oxygen from the catalyst surface. A saturation was performed with CO_2 (5% CO_2–95% He, LLC "NII KM") at 60 °C for 24 min. The physically adsorbed CO_2 was removed at 102 °C in the flow of He (30 mL/min) for 60 min. An analysis was performed in the flow of He in the temperature range of 100–800 °C (heating rate 7 °C/min). The registration of desorbed CO_2 was carried out with a thermal conductivity detector.

2.4. Plasma-Catalytic Experiments

The investigation of catalytic activity was carried out using an experimental plasma-catalytic unit (Figure 1). A quartz tube (16 mm diameter, 2 mm wall thickness) was used as a reactor. A steel rod with a screw thread (8 mm diameter) was applied as an inner (high voltage) electrode. A stainless steel mesh (0.5 mm mesh size, 80 mm length) was placed on the outer wall of the quartz tube and served as a ground electrode. The discharge gap was 4 mm. The catalyst was placed into the reactor and fixed with mineral wool on both ends of the catalyst bed. The ceramic beads were used as an inert packing material for comparison with the catalysts prepared. Carbon dioxide was injected into the reactor using a mass flow gas controller RRG-20 (LLC "Eltochpribor", Russia). The CO_2 flow rate was kept at 17 mL/min for all experiments. A high voltage generator with 23 kHz frequency was used as a power source. The discharge voltage and current were registered with a TDS 2012B oscilloscope (Tektronix, Beaverton, OR, USA). Plasma-absorbed power was calculated from the area of the Lissajous figure and was 5–9 W depending on the catalyst type being put inside the reactor. Gaseous products were analyzed using a gas chromatograph PIA (LLC "NPF MEMS", Samara, Russia), with a thermal conductivity detector, and equipped with Hayesep N adsorbent column (l = 2 m) and molecular sieves 13Å column (l = 2 m).

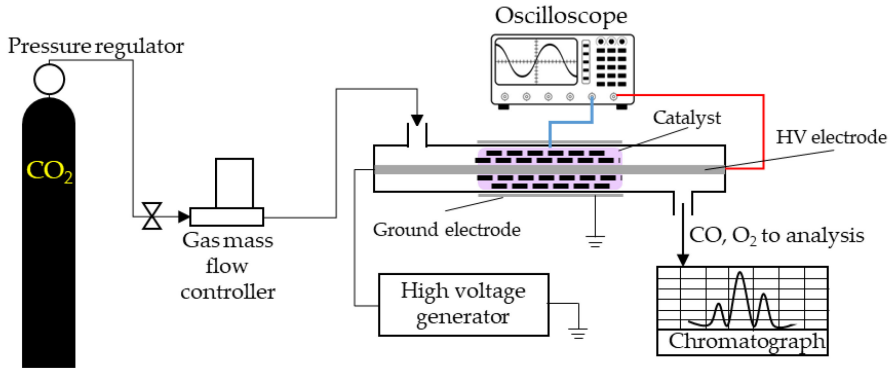

Figure 1. A schematic of the experimental setup.

The conversion of CO_2 (X) was calculated as

$$X(CO_2)(\%) = \frac{\nu(CO_2)_{inlet} - \nu(CO_2)_{outlet}}{\nu(CO_2)_{inlet}} \times 100\% \quad (2)$$

where $\nu(CO_2)_{inlet}$ is the quantity of CO_2 which is put into the reactor, $\nu(CO_2)_{outlet}$ is the quantity of CO_2 in the gas sample.

Plasma-absorbed power was calculated from the Volt-Coulomb characteristic (Lissajous figure) of the discharge as [33,34]:

$$P = fW = f\int_{t_0-\frac{T}{2}}^{t_0+\frac{T}{2}} u(t)i(t)dt = fC_n\int_{t_0-\frac{T}{2}}^{t_0+\frac{T}{2}} u(t)du_c(t) = fC_nA \quad (3)$$

where $u(t)$ is the discharge voltage, $i(t)$ is the discharge current, C_n is the value of the capacitor included in series with the discharge tube, $u_c(t)$ is a voltage on the C_n, T is the period of the applied voltage, f is a frequency of the applied voltage, A is the area of the Lissajous figure.

The energy efficiency of the process was calculated as

$$\eta(\%) = \frac{X(\%)G_{in}^{CO_2}\Delta H_{298,K}^0}{P} \times 100\%, \quad (4)$$

where $G_{in}^{CO_2}$ is inlet CO_2 flow rate [mol/s], $\Delta H_{298,K}^0$ is the enthalpy of C=O bond cleavage, which is 283 kJ/mol.

3. Results and Discussion

3.1. Catalyst Characterization

The catalysts obtained were characterized by physicochemical methods. The composition of the catalysts was analyzed using XRF spectroscopy (Table 2). It is stated from the analysis results that the content of the oxide in the samples is close to the calculated data.

Table 2. The content of oxides in the samples and the textural characteristics of the prepared catalysts.

Sample	Oxide Content, wt.%					Textural Characteristics		
	Al_2O_3	MgO	CeO_2	SiO_2	CaO	S_{BET}, m^2/g	V_{pores}, cm^3/g	d_{pores}, nm
Al	99	-	-	1	-	202	0.50	8.6
Ce–Al	88.7	-	10.5	0.8	-	190	0.43	8.5
Mg–Al	87.2	12	-	0.8	-	181	0.43	8.1
MgCe–Al	75.7	11.8	11.7	0.8	-	161	0.33	7.6
Ce20–Al	79.3	-	19.7	1	-	169	0.37	8
CaCe–Al	78.5	-	11.8	0.5	9.2	140	0.30	7.5

The textural characteristics were determined by a low-temperature N_2 adsorption-desorption analysis. The adsorption isotherms (Figure 2a) correspond to type IV and possess a hysteresis loop (in the range of p/p_0 = 0.6–0.9), which means mesopores are present in the sample. The surface area of the catalysts decreases when the metal oxides are introduced, and so does the pore volume (Table 2). This can be attributed to partial pore blockage with metal oxide particles. It should be noted that the catalysts possess the unimodal narrow pore size distribution (Figure 2b), which is preserved with different oxide loading.

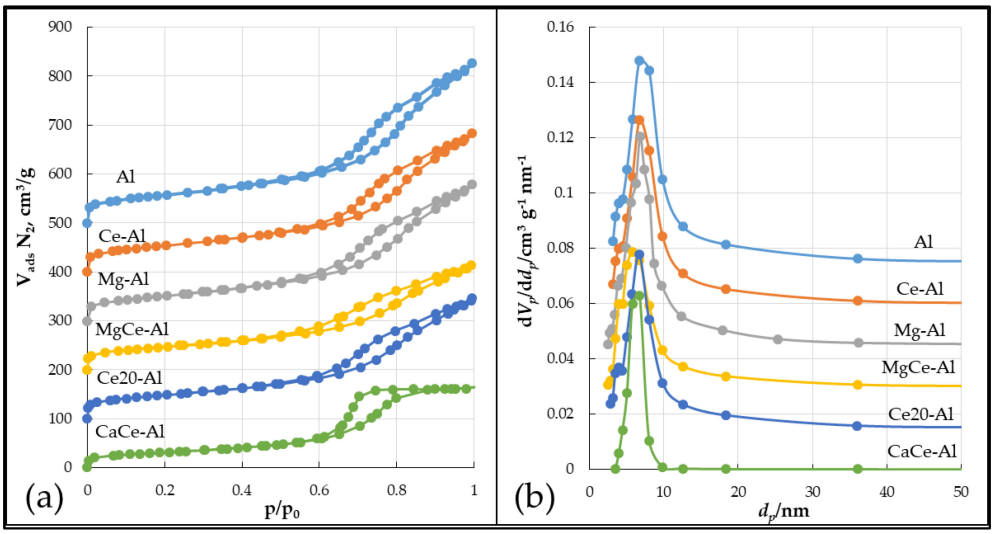

Figure 2. The low-temperature N_2 adsorption isotherms (**a**); and pore size distribution (**b**).

The phase composition of the catalysts was determined using an X-ray diffraction analysis. It is seen from Figure 3 that the CeO_2 phase in the samples is of a high crystallinity degree (narrow diffraction peak at 2θ = 28.6°). There are no mixed or double oxides present in the samples.

The surface of the Ce–Al and MgCe–Al samples was also analyzed by X-ray photoelectron spectroscopy (Figure 4). Raw spectra were deconvoluted to obtain information about the Ce oxide composition. The peaks assigned u‴ (917 eV), u″ (907 eV), u (900.5 eV), v‴ (898 eV), v″ (888 eV), and v (882.1 eV) correspond to the CeO_2, while u′ (903 eV) and v′ (885 eV) correspond to Ce_2O_3 [35]. It is stated from the XPS analysis that the catalysts prepared contained mostly CeO_2 oxide (83% for Ce–Al and 84% for MgCe-Al). Deconvo-

luted peak characteristics (peak position, full width at half maximum, and peak area) are demonstrated in Table S1.

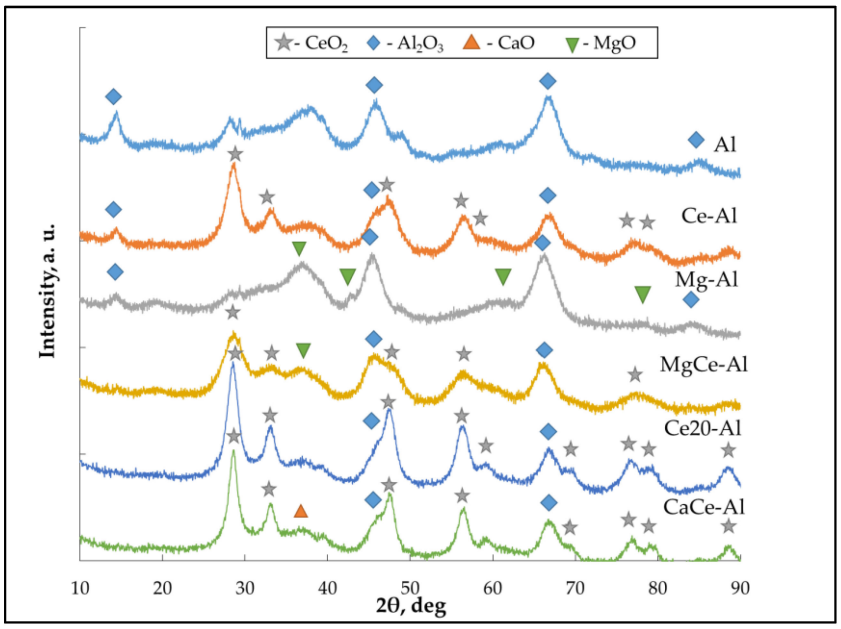

Figure 3. The powder X-ray diffraction of prepared catalysts.

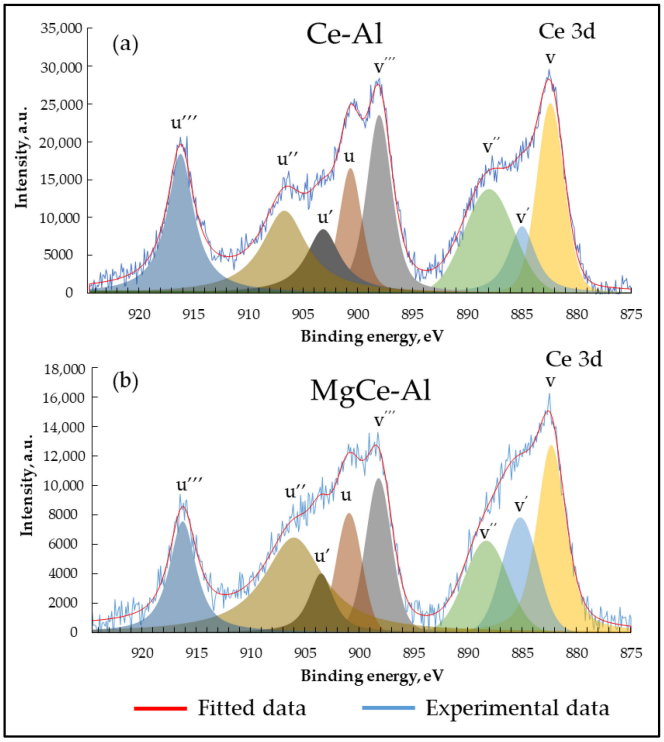

Figure 4. The X-ray photoelectron spectra of the Ce–Al (**a**) and MgCe–Al (**b**) samples.

3.2. The Plasma-Catalytic Performance

The plasma-catalytic CO_2 decomposition tests were carried out in a continuous gas flow mode. The input power was calculated based on the Lissajous figures obtained (Figure 5). It can be seen from Figure 5 that in the absence of any packing material inside the discharge zone, the Lissajous figure is broad, and it shrinks when the inert beads or

catalyst are packed inside. This can be related to the difference in dielectric properties of the materials.

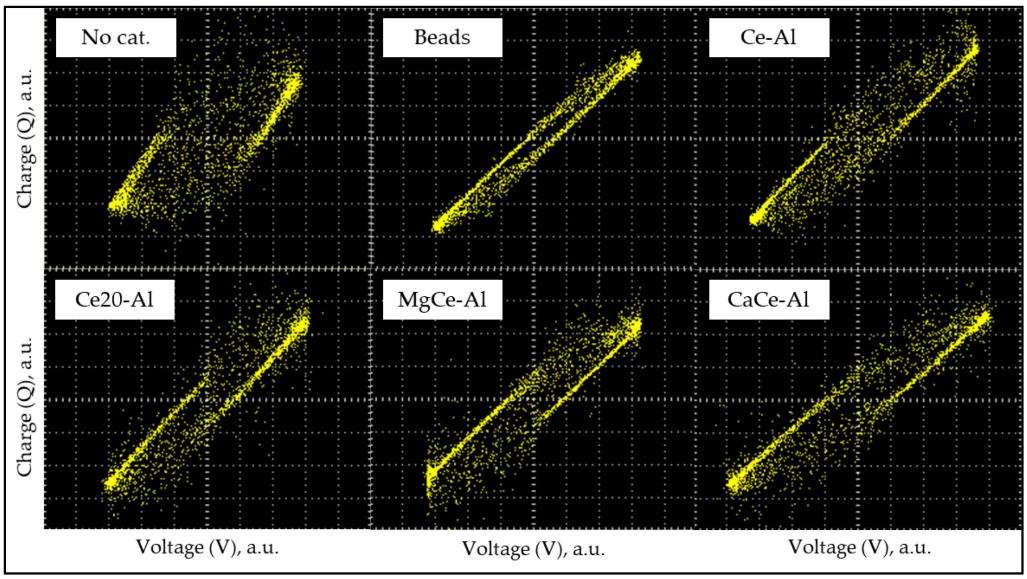

Figure 5. The Lissajous figures obtained during the CO_2 decomposition experiments both with and without catalysts.

At the beginning of each plasma-catalytic process, some amount of condensed liquid was observed at the outlet end of the quartz tube. This liquid is attributed to the water which is absorbed by hygroscopic MgO and Al_2O_3 substances and then evaporated during the first 60 min of run (Figure 6). When all of the adsorbed water is evaporated, the steady-state CO_2 decomposition process is observed.

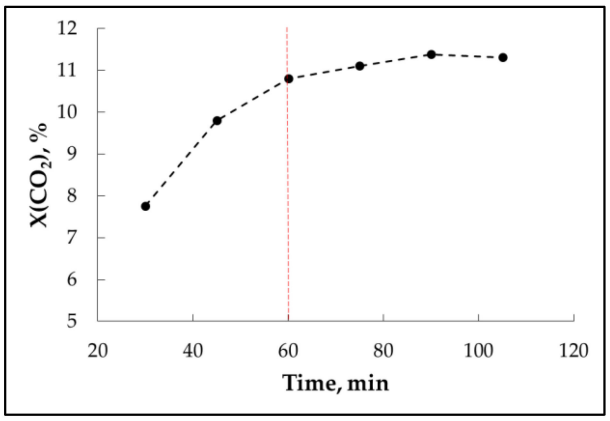

Figure 6. The plasma-catalytic CO_2 conversion in the presence of Mg–Al catalyst. The red dashed line represents the time, after which steady-state CO_2 decomposition is observed.

The dissociation of the CO_2 molecule can be accomplished either with CO formation or C formation as the main carbon product. However, under dielectric barrier discharge plasma conditions, solid carbon formation is quite unlikely, as this reaction requires extremely high temperatures (6000–7000 °C) [36]. To prove that CO was the main product of CO_2 decomposition, the $[CO]/[O_2]$ ratio was calculated from the gas chromatography results. The calculated ratio was close to 2 (1.9–2.1) which corresponds to only CO formation during CO_2 dissociation.

During the plasma-catalytic experiments, the catalysts were compared by the characteristics of the CO_2 conversion degree (X) and energy efficiency (η) (Figure 7a,c). It could be seen from the results that the lowest CO_2 conversion and energy efficiency values are

achieved in the absence of any packing material in the reactor. The introduction of inert ceramic beads changes the electric properties of the barrier discharge (Figure 5) but does not lead to a significant increase in CO_2 conversion (Figure 7a). The highest CO_2 conversion values are reached in the presence of Ce–Al, Ce20–Al and MgCe–Al samples. The catalyst stability test is performed using the MgCe–Al sample (Figure 7d). It is seen that the conversion of CO_2 reaches a maximum at 75 min of run and does not decrease significantly up to 120 min. The energy efficiency was calculated based on the CO_2 conversion/input power ratio. In the presence of MgCe–Al, the highest energy efficiency is achieved which means less energy input is needed for a higher conversion value. The highest performance of CO_2 decomposition in the presence of the MgCe–Al sample could be proof of the initial hypothesis of MgO and CeO_2 properties combined in a single catalyst. However, in the presence of CaCe–Al (which also contains basic oxide CaO), the conversion of CO_2 is even lower than that in the presence of Al_2O_3, without any additional metal oxides. To explain this, additional results were obtained that will be discussed in the next section.

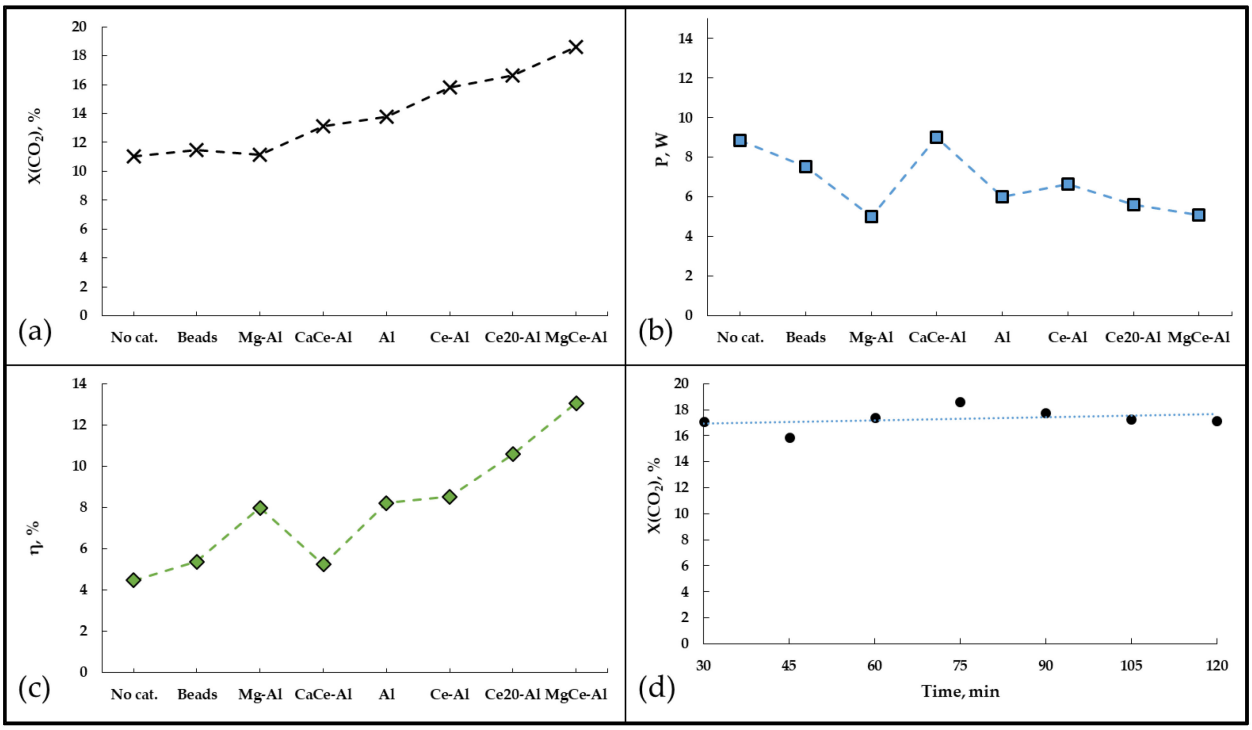

Figure 7. The results of the plasma-catalytic decomposition of CO_2 in the presence of the catalysts prepared: (**a**) conversion of CO_2; (**b**) input power; (**c**) energy efficiency; (**d**) MgCe–Al catalyst stability test during 2 h of run.

To investigate the reusability of the catalysts, the MgCe-Al sample was chosen as the catalyst, which showed the highest CO_2 conversion activity. The reusability tests were carried out in the same reactor for five runs without any pretreatment or regeneration of the catalyst before each run. The results (Table 3) show that the activity of the catalyst does not change significantly during five tests, so the catalyst can be used several times without any regeneration.

The plasma-catalytic experiment results obtained were compared with previously published data on CO_2 decomposition (Table 4). It should be noted that a direct comparison of the experiment results is quite difficult because the operating parameters (power, CO_2 flow rate) and reactor design (discharge gap, electrode materials, etc.) are dissimilar in each study. However, it can be seen that under significantly lower input power (5.1–8.9 W), comparable conversions are achieved in the presence of our catalytic systems. It should be noted that in the work [31] the CaO sample showed an inferior plasma-catalytic CO_2 performance, which

is consistent with our study. However, no explanation of this phenomenon was provided in that study.

Table 3. The reusability tests of the MgCe-Al sample during five cycles.

No. of Run	X (CO_2), %	Energy Efficiency, %
1	18.3	14.4
2	17.8	11.8
3	18.6	13.0
4	18.0	13.3
5	18.3	13.5

Table 4. A comparison of the DBD plasma-catalytic CO_2 decomposition using Ce and Mg catalysts.

Catalyst	Input Power, W	Energy Efficiency, %	X (CO_2), %	Source
Mo/CeO_2	13.5	14.3	23.2	[28]
MgO	60	6.1	24	[31]
MgAl–LDH	60	5.8	20	
CaO	60	4.8	19	
ZrO_2–CeO_2	50	2.4	64	[37]
5 wt.% Fe_2O_3–5 wt.% CeO_2/Al_2O_3	15	10.2	24.5	[38]
10 wt.% CeO_2/Al_2O_3	15	15.7	28.5	
CeO_2 coated on frosted quartz	26.5	2.1	26.3	[39]
CeO_2-cubes	15–20	3.8	16	[40]
CeO_2-rodes	15–20	3.7	16	
CeO_2-hexagons	15–20	3.1	20	
Ce–Al	6.6	8.5	15.8	This work
Ce20–Al	5.6	10.6	16.6	This work
MgCe–Al	5.1	13	18.6	This work
CaCe–Al	8.9	5.2	13.2	This work

3.3. Catalyst Characterization after the Plasma-Catalytic Reaction

The catalysts after the reaction (spent catalysts) were characterized by physicochemical methods to estimate how the plasma-catalytic CO_2 decomposition process affects the properties of the catalysts. When comparing the adsorption isotherms (Figure 8), it is clear that the textural characteristics do not change after the reaction. The values of S_{BET}, V_{pores}, and d_{pores} of the spent catalysts (Table 5) are close to their initial ones (Table 2) and are within the error of the method. The oxide content (Table 5) corresponds to those of the catalysts prepared, which means no carbon deposition occurred during the CO_2 decomposition.

The phase content also remains unchanged after the reaction (Figure 9). As can be seen from the diffractograms, spent catalysts did not contain any new phases; the intensity of the diffraction patterns is comparable with that of the catalysts before the reaction. The average size of the crystallites in the catalysts before and after the reaction was calculated using the Scherrer equation [41]. It is seen from Table 6 that the average size of the crystallite remained unchanged for all of the phases. It indicates that the crystallites did not aggregate under mild DBD conditions.

The oxidation state of the Ce in the Ce–Al and MgCe–Al spent samples was analyzed by Ce 3d XPS (Figure 10). It was observed that the CeO_2 state is still predominant, but the Ce_2O_3 state quantity is enhanced compared to that found in the catalysts before the reaction (peak position, full width at half maximum, and peak area of the deconvoluted spectra are provided in Table S2). Based on the Ce^{3+} peak area proportion in the spectrum,

the oxygen vacancies content was calculated ($Ce^{3+}/(Ce^{3+} + Ce^{4+})$ [42]. It was revealed that the oxygen vacancies content in the fresh Ce-Al and MgCe-Al catalysts were 0.17 and 0.16, correspondingly, and were enhanced after the reaction (0.27 for spent Ce–Al and 0.29 for spent MgCe–Al). These results indicate the oxygen state modification during the plasma-catalytic process, which helps efficient CO_2 adsorption with subsequent decomposition.

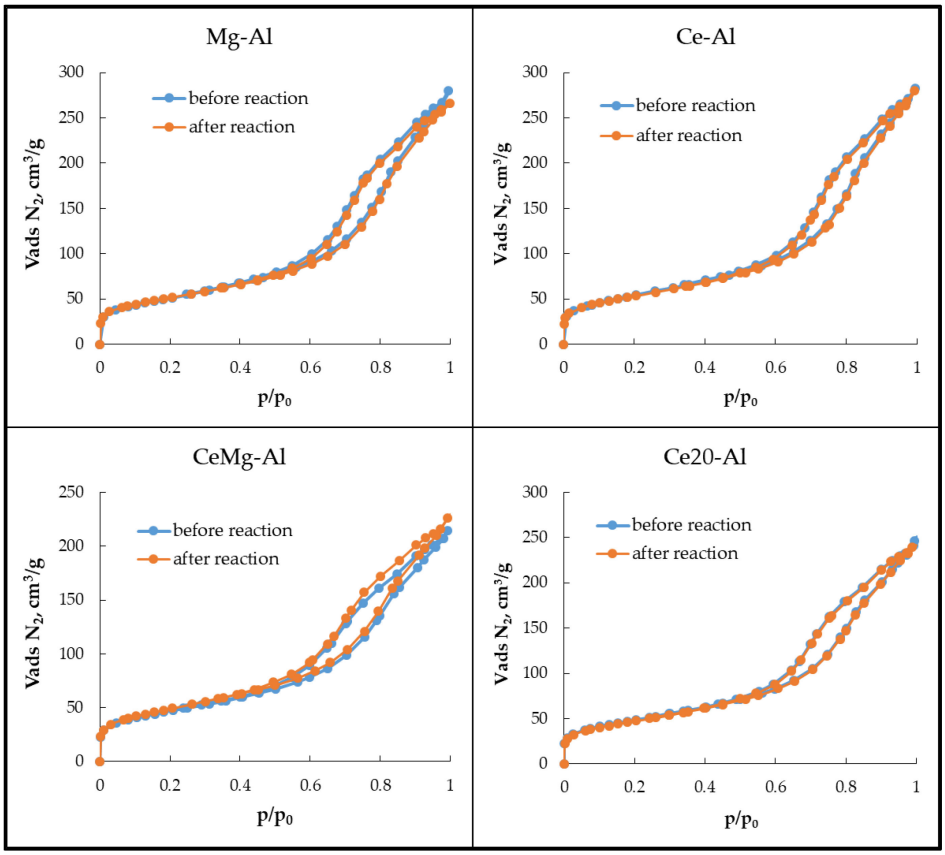

Figure 8. The adsorption isotherms obtained by low-temperature N_2 adsorption for the catalysts before and after the reaction.

Table 5. The oxide content and textural characteristics in the spent catalysts.

Sample	Oxide Content, wt.%					Textural Characteristics		
	Al_2O_3	MgO	CeO_2	SiO_2	CaO	S_{BET}, m^2/g	V_{pores}, cm^3/g	d_{pores}, nm
Ce–Al	88.5	-	11	0.5	-	184	0.43	8.6
Mg–Al	87	12.5	-	0.5	-	178	0.40	8.1
MgCe–Al	77	12.8	9.4	0.8	-	171	0.35	7.7
Ce20–Al	79	-	20.5	0.5	-	165	0.36	7.1
CaCe–Al	78	-	12.1	0.5	9.4	127	0.24	6.7

Table 6. The average crystallite size of the fresh and spent catalysts was determined from the XRD analysis.

	Sample							
	Mg–Al		Ce–Al		MgCe–Al		Ce20–Al	
	Fresh	Spent	Fresh	Spent	Fresh	Spent	Fresh	Spent
MgO crystallite size, nm	1.5 ± 0.2	1.4 ± 0.1	-	-	2.1	2.2	-	-
CeO_2 crystallite size, nm	-	-	3.3 ± 0.3	3.6 ± 0.5	3.1 ± 0.4	3.1 ± 0.5	4.5 ± 0.8	4.6 ± 0.7

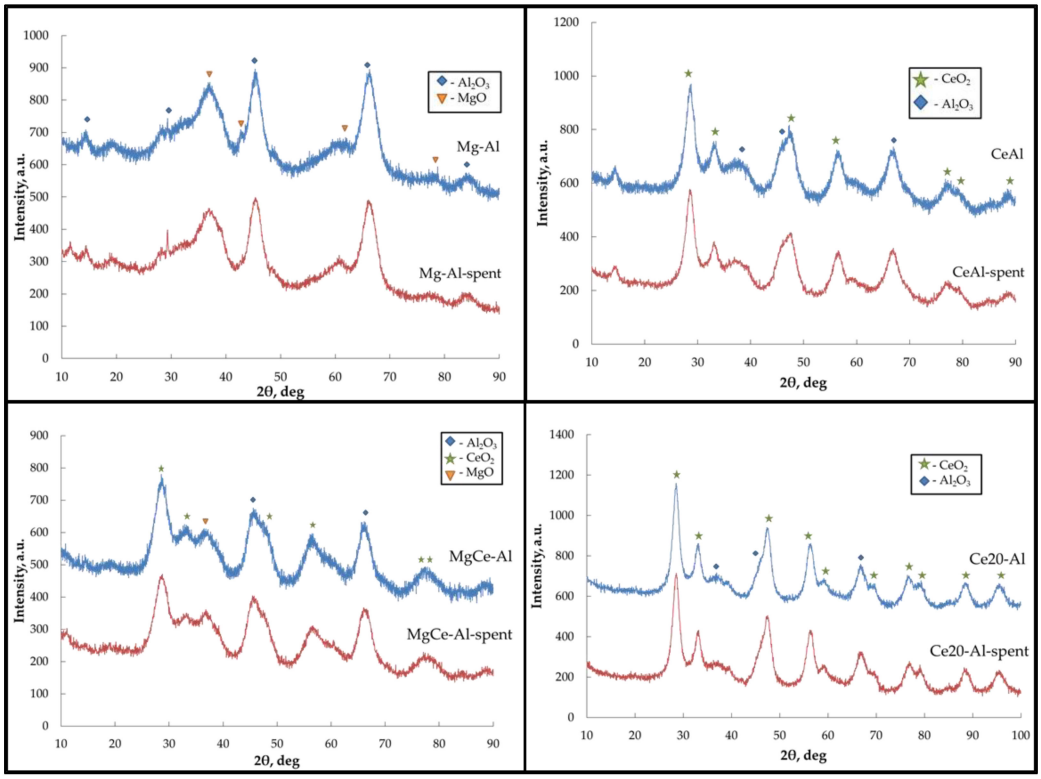

Figure 9. A comparison of the diffractograms of the catalysts before and after the reaction.

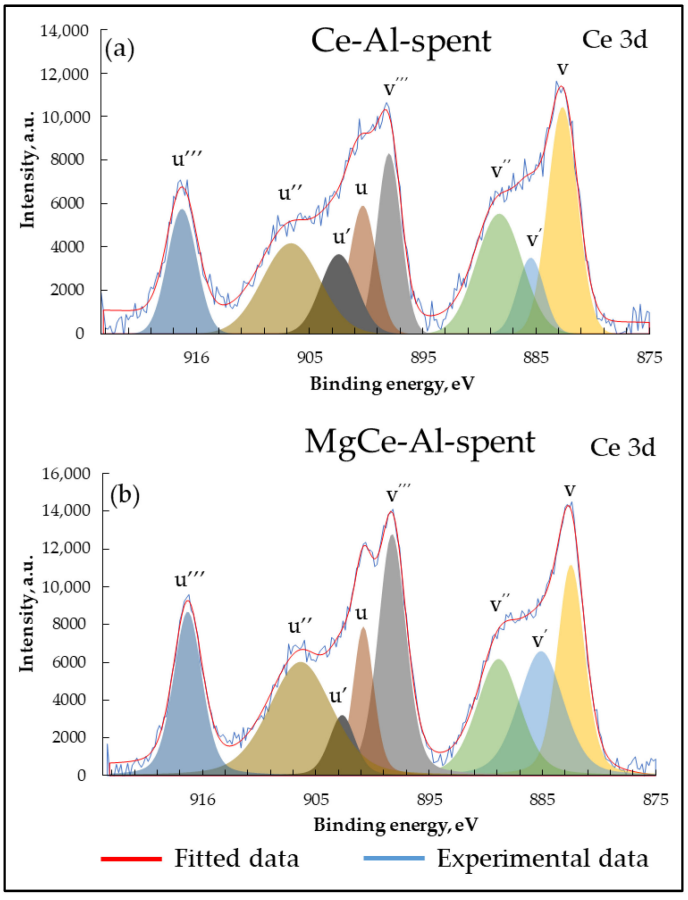

Figure 10. The X-ray photoelectron spectra of Ce–Al (**a**) and MgCe–Al (**b**) samples after the reaction.

To investigate the influence of the MgO or CaO addition to the CeO_2/Al_2O_3 samples, a basicity analysis was carried out using the TPD-CO_2 technique. It is seen in Figure 11 that TPD-CO_2 patterns include two desorption peaks. The low-temperature peak corresponds to the weak basic sites, while the high-temperature peak corresponds to the strong basic sites. From Table 7, it is clear that Mg-Al and CaCe–Al are considered as the samples possessing the highest basicity. However, their plasma-catalytic activity is the lowest, which is inconsistent with their basicity. The probable explanation can be made based on the strong basic site concentration. The desorption of CO_2 from the strong basic sites occurs at a high temperature, which cannot be reached during the dielectric barrier discharge conditions. It means that under plasma-catalytic conditions better CO_2 conversion is achieved using catalysts with moderate basicity. This observation is per the work [43] where MgO-based sorbents for CO_2 capture are demonstrated as better candidates compared to CaO, due to the lower capture temperature.

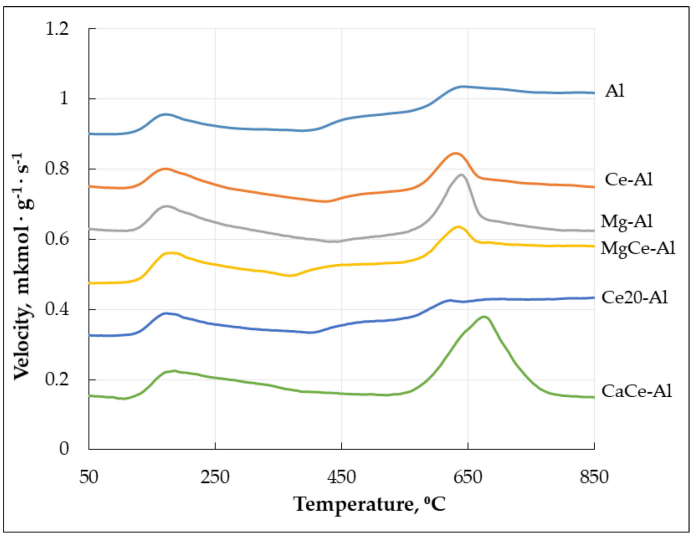

Figure 11. The TPD-CO_2 patterns for synthesized catalysts.

Table 7. The quantity of the basic sites, as determined by TPD-CO_2.

Sample	Basic Sites Concentration, mkmol/g		
	Weak (50–250 °C)	Strong (500–700 °C)	Total
Al	35	-	35
Ce–Al	32	53	85
Mg–Al	69	96	165
MgCe–Al	66	52	118
Ce20–Al	51	-	51
CaCe–Al	83	190	273

Thus, from a practical point of view, combined MgO–CeO_2 catalysts may be applied for CO_2 decomposition using plasma catalysis. However, this process certainly needs further research and development.

4. Conclusions

The present work shows that the combination of MgO and CeO_2 in a single catalyst is beneficial for plasma-catalytic CO_2 decomposition under mild conditions. The dominant role in the CO_2 dissociation process is assigned to the CeO_2 rather than the MgO. When the single oxide catalysts are compared (Mg–Al vs. Ce–Al), the catalyst with CeO_2 shows better plasma-catalytic performance (CO_2 conversion is 11.1% and 15.8% in the presence of Mg–Al and Ce–Al, correspondingly). Despite this, the MgO and CeO_2 combination shows superior CO_2 conversion due to the increase in weak basic sites, which facilitate

CO_2 adsorption on the catalyst surface. The CaO-CeO_2 combination in a catalyst leads to a decrease in CO_2 conversion and energy efficiency, which can be related to the presence of strong basic sites from which CO_2 cannot be desorbed under reaction conditions.

The results obtained in this work may help in further developing efficient plasma-catalytic CO_2 decomposition methods. The practical impact of this work consists of a search for appropriate catalyst design. The MgO–CeO_2 combination in the catalyst for such a process seems promising and needs to be more deeply investigated. For example, different MgO–CeO_2 molar ratios will be tested in CO_2 decomposition, as well as bulk metal oxides (without Al_2O_3 support) in future work.

Supplementary Materials: The following supporting information can be downloaded at: https://www.mdpi.com/article/10.3390/pr11051553/s1, Table S1: Peak position, full width at half maximum (FWHM) and peak area of the fitted XPS spectra of the Ce–Al and MgCe–Al samples (before the reaction); Table S2: Peak position, full width at half maximum (FWHM) and peak area of the fitted XPS spectra of the Ce–Al-spent and MgCe–Al-spent samples (after the reaction).

Author Contributions: Conceptualization O.G. and A.M.; methodology O.G.; validation O.G.; formal analysis O.G.; investigation O.G.; writing—original draft preparation, O.G.; writing—review and editing A.M.; visualization, O.G.; project administration, A.M.; funding acquisition, A.M. All authors have read and agreed to the published version of the manuscript.

Funding: This research was funded by Russian Science Foundation (grant no. 17-73-30046P).

Data Availability Statement: Not applicable.

Acknowledgments: The authors are grateful to Lebedev Yu. A. for help in preparing this article. This work was performed using the equipment of the Shared Research Center Analytical center of deep oil processing and petrochemistry of the A.V. Topchiev Institute of Petrochemical Synthesis RAS.

Conflicts of Interest: The authors declare no conflict of interest.

References

1. Hossain, M.F. Extreme Level of CO_2 Accumulation into the Atmosphere Due to the Unequal Global Carbon Emission and Sequestration. *Water Air Soil Pollut.* **2022**, *105*, 233. [CrossRef]
2. Yoro, K.O.; Daramola, M.O. CO_2 emission sources, greenhouse gases, and the global warming effect. In *Advances in Carbon Capture*; Rahimpour, M.R., Farsi, M., Makarem, M.A., Eds.; Woodhead Publishing: Sawston, UK, 2020; pp. 3–28. [CrossRef]
3. Vega, F.; Baena-Moreno, F.M.; Gallego Fernández, L.M.; Portillo, E.; Navarrete, B.; Zhang, Z. Current status of CO_2 chemical absorption research applied to CCS: Towards full deployment at industrial scale. *Appl. Energy* **2020**, *260*, 114313. [CrossRef]
4. Yang, H.; Zhang, C.; Gao, P.; Wang, H.; Li, X.; Zhong, L.; Wei, W.; Sun, Y. A review of the catalytic hydrogenation of carbon dioxide into value-added hydrocarbons. *Catal. Sci. Technol.* **2017**, *7*, 4580–4598. [CrossRef]
5. Salehizadeh, H.; Ning, Y.; Farnood, R. Recent advances in microbial CO_2 fixation and conversion to value-added products. *Chem. Eng. J.* **2020**, *390*, 124584. [CrossRef]
6. Aerts, R.; Somers, W.; Bogaerts, A. Carbon Dioxide Splitting in a Dielectric Barrier Discharge Plasma: A Combined Experimental and Computational Study. *Chem. Sus. Chem.* **2015**, *8*, 702–716. [CrossRef] [PubMed]
7. Aerts, R.; Martens, T.; Bogaerts, A. Influence of Vibrational States on CO_2 Splitting by Dielectric Barrier Discharges. *J. Phys. Chem.* **2012**, *116*, 23257–23273. [CrossRef]
8. Batukaev, T.S.; Bilera, I.V.; Krashevskaya, G.V.; Lebedev, Y.A.; Nazarov, N.A. CO_2 Decomposition in Microwave Discharge Created in Liquid Hydrocarbon. *Plasma* **2023**, *6*, 115–126. [CrossRef]
9. Chen, G.; Snyders, R.; Britun, N. CO_2 conversion using catalyst-free and catalyst-assisted plasma-processes: Recent progress and understanding. *J. CO2 Util.* **2021**, *49*, 101557. [CrossRef]
10. Shah, Y.T.; Verma, J.; Katti, S.S. Plasma activated catalysis for carbon dioxide dissociation: A review. *J. Indian Chem. Soc.* **2021**, *98*, 100152. [CrossRef]
11. Chen, G.; Georgieva, V.; Godfroid, T.; Snyders, R.; Delplancke-Ogletree, M.-P. Plasma assisted catalytic decomposition of CO_2. *Appl. Catal. B Environ.* **2016**, *190*, 115–124. [CrossRef]
12. Zhang, K.; Zhang, G.; Liu, X.; Phan, A.N.; Luo, K.A. Study on CO_2 decomposition to CO and O_2 by the combination of catalysis and dielectric-barrier discharges at low temperatures and ambient pressure. *Ind. Eng. Chem. Res.* **2017**, *56*, 3204–3216. [CrossRef]
13. Lebedev, Y.A.; Shakhatov, V.A. Decomposition of CO_2 in Atmospheric-Pressure Barrier Discharge (Analytical Review). *Plasma Phys. Rep.* **2022**, *48*, 693–710. [CrossRef]
14. Ray, D.; Subrahmanyam, C. CO_2 decomposition in a packed DBD plasma reactor: Influence of packing materials. *RSC Adv.* **2016**, *6*, 39492–39499. [CrossRef]

15. Carreon, M.L. Plasma catalysis: A brief tutorial. *Plasma Res. Express* **2019**, *1*, 043001. [CrossRef]
16. Kogelschatz, U. Dielectric-barrier discharges: Their history, discharge physics, and industrial applications. *Plasma Chem. Plasma Process.* **2003**, *23*, 1–46. [CrossRef]
17. Chen, H.L.; Lee, H.M.; Chen, S.H.; Chao, Y.; Chang, M.B. Review of plasma catalysis on hydrocarbon reforming for hydrogen production—Interaction, integration, and prospects. *Appl. Catal. B* **2008**, *85*, 1–9. [CrossRef]
18. Xu, S.; Whitehead, C.J.; Martin, P.A. CO_2 conversion in a non-thermal, barium titanate packed bed plasma reactor: The effect of dilution by Ar and N_2. *Chem. Eng. J.* **2017**, *327*, 764–773. [CrossRef]
19. Michielsen, I.; Uytdenhouwen, Y.; Pype, J.; Michielsen, B.; Mertens, J.; Reniers, F.; Meynen, V.; Bogaerts, A. CO_2 dissociation in a packed bed DBD reactor: First steps towards a better understanding of plasma catalysis. *Chem. Eng. J.* **2017**, *326*, 477–488. [CrossRef]
20. Yu, Q.; Kong, M.; Liu, T.; Fei, J.; Zheng, X. Characteristics of the decomposition of CO_2 in a dielectric packed bed plasma reactor. *Plasma Chem. Plasma Process.* **2012**, *32*, 153–163. [CrossRef]
21. Mei, D.; Tu, X. Atmospheric pressure non-thermal plasma activation of CO_2 in a packed-bed dielectric barrier discharge reactor. *Chem. Phys. Chem.* **2017**, *18*, 3253–3259. [CrossRef]
22. Yang, C.; Lu, Y.; Zhang, L.; Kong, Z.; Yang, T.; Tao, L.; Zou, Y.; Wang, S. Defect Engineering on CeO_2-Based Catalysts for Heterogeneous Catalytic Applications. *Small Struct.* **2021**, *2*, 2100058. [CrossRef]
23. Xie, Y.; Wu, J.; Jing, G.; Zhang, H.; Zeng, S.; Tian, X.; Zou, X.; Wen, J.; Su, H.; Zhong, C.-J.; et al. Structural origin of high catalytic activity for preferential CO oxidation over CuO/CeO_2 nanocatalysts with different shapes. *Appl. Catal. B* **2018**, *239*, 665. [CrossRef]
24. Yang, C.; Li, Q.; Xia, Y.; Lv, K.; Li, M. Enhanced visible-light photocatalytic CO_2 reduction performance of $Znln_2S_4$ microspheres by using CeO_2 as cocatalyst. *Appl. Surf. Sci.* **2019**, *464*, 388–395. [CrossRef]
25. Yu, J.; Wang, J.; Long, X.; Chen, L.; Cao, Q.; Wang, J.; Qiu, C.; Lim, J.; Yang, S. Formation of FeOOH Nanosheets Induces Substitutional Doping of CeO_{2-x} with High-Valence Ni for Efficient Water Oxidation. *Adv. Energy Mater.* **2021**, *11*, 2002731. [CrossRef]
26. Wang, A.; Zheng, Z.; Wang, H.; Chen, Y.; Luo, C.; Liang, D.; Hu, B.; Qiu, R.; Yan, K. 3D hierarchical H_2-reduced Mn-doped CeO_2 microflowers assembled from nanotubes as a high-performance Fenton-like photocatalyst for tetracycline antibiotics degradation. *Appl. Catal. B* **2020**, *277*, 119171. [CrossRef]
27. Di Sarli, V.; Landi, G.; Di Benedetto, A.; Lisi, L. Synergy Between Ceria and Metals (Ag or Cu) in Catalytic Diesel Particulate Filters: Effect of the Metal Content and of the Preparation Method on the Regeneration Performance. *Top. Catal.* **2021**, *64*, 256–269. [CrossRef]
28. Wang, L.; Du, X.; Yi, Y.; Wang, H.; Gul, M.; Zhu, Y.; Tu, X. Plasma-enhanced direct conversion of CO_2 to CO over oxygen-deficient Mo-doped CeO_2. *Chem. Commun.* **2020**, *56*, 14801–14804. [CrossRef] [PubMed]
29. Mei, D.; He, Y.; Liu, S.; Yan, J.; Tu, X. Optimization of CO_2 conversion in a cylindrical dielectric barrier discharge reactor using design of experiments. *Plasma Process. Polym.* **2016**, *13*, 544–556. [CrossRef]
30. Duan, X.; Hu, Z.; Li, Y.; Wang, B. Effect of dielectric packing materials on the decomposition of carbon dioxide using DBD microplasma reactor. *AIChE J.* **2015**, *61*, 898–903. [CrossRef]
31. Wang, B.; Li, X.; Wang, X.; Zhang, B. Effect of filling materials on CO_2 conversion with a dielectric barrier discharge reactor. *J. Environ. Chem. Eng.* **2021**, *9*, 106370. [CrossRef]
32. Lebedev, Y.A.; Golubev, O.V.; Batukaev, T.S.; Maximov, A.L. Decomposition of CO_2 in a barrier discharge in the presence of cerium oxide catalysts. *Tech. Phys. Lett.* 2023, *in press*.
33. Lu, N.; Liu, N.; Zhang, C.; Su, Y.; Shang, K.; Jiang, N.; Li, J.; Wu, Y. CO_2 conversion promoted by potassium intercalated g-C_3N_4 catalyst in DBD plasma system. *Chem. Eng. J.* **2021**, *417*, 129283. [CrossRef]
34. Holub, M. On the measurement of plasma power in atmospheric pressure DBD plasma reactors. *Int. J. Appl. Electromagn. Mech.* **2012**, *39*, 81–87. [CrossRef]
35. Zhang, F.; Wang, P.; Koberstein, J.; Khalid, S.; Chan, S.-W. Cerium oxidation state in ceria nanoparticles studied with X-ray photoelectron spectroscopy and absorption near edge spectroscopy. *Surf. Sci.* **2004**, *563*, 74–82. [CrossRef]
36. Centi, G.; Perathoner, S.; Papanikolaou, G. Plasma assisted CO_2 splitting to carbon and oxygen: A concept review analysis. *J. CO2 Util.* **2021**, *54*, 101775. [CrossRef]
37. Li, J.; Zhu, S.; Lu, K.; Ma, C.; Yang, D.; Yu, F. CO_2 conversion in a coaxial dielectric barrier discharge plasma reactor in the presence of mixed ZrO_2–CeO_2. *J. Environ. Chem. Eng.* **2021**, *9*, 104654. [CrossRef]
38. Ashford, B.; Wang, Y.; Poh, C.-K.; Chen, L.; Tu, X. Plasma-catalytic conversion of CO_2 to CO over binary metal oxide catalysts at low temperatures. *Appl. Catal. B.* **2020**, *276*, 119110. [CrossRef]
39. Xia, M.; Ding, W.; Shen, C.; Zhang, Z.; Liu, C. CeO_2-Enhanced CO_2 Decomposition via Frosted Dielectric Barrier Discharge Plasma. *Ind. Eng. Chem. Res.* **2022**, *61*, 10455–10460. [CrossRef]
40. Ji, H.; Lin, L.; Chang, K. Plasma-assisted CO_2 decomposition catalyzed by CeO_2 of various morphologies. *J. CO_2 Util.* **2023**, *68*, 102351. [CrossRef]
41. Liu, R.; Leshchev, D.; Stavitski, E.; Juneau, M.; Agwara, J.N.; Porosoff, M.D. Selective hydrogenation of CO_2 and CO over potassium promoted Co/ZSM-5. *Appl. Catal. B* **2021**, *284*, 119787. [CrossRef]

42. Zheng, X.; Li, Y.; Zhang, L.; Shen, L.; Xiao, Y.; Zhang, Y.; Jiang, L. Insight into the effect of morphology on catalytic performance of porous CeO_2 nanocrystals for H_2S selective oxidation. *Appl. Catal. B* **2019**, *252*, 98–110. [CrossRef]
43. Yu, H.; Wang, X.; Shu, Z.; Fujii, M.; Song, C. Al_2O_3 and CeO_2-promoted MgO sorbents for CO_2 capture at moderate temperatures. *Front. Chem. Sci. Eng.* **2018**, *12*, 89–93. [CrossRef]